Low processing temperatures explored in Sb_2S_3 solar cells by close-spaced sublimation and analysis of bulk and interface related defects

R. Krautmann [a],[**], N. Spalatu [a],[*], R. Josepson [b], R. Nedzinskas [c], R. Kondrotas [c], R. Gržibovskis [d], A. Vembris [d], M. Krunks [a], I. Oja Acik [a]

[a] *Department of Materials and Environmental Technology, Tallinn University of Technology, Ehitajate tee 5, 19086, Tallinn, Estonia*
[b] *Division of Physics, Tallinn University of Technology, Ehitajate tee 5, 19086, Tallinn, Estonia*
[c] *State Research Institute Center for Physical Sciences and Technology, Saulėtekio Avenue 3, 10257, Vilnius, Lithuania*
[d] *Institute of Solid State Physics, University of Latvia, Kengaraga iela 8, 1063, Riga, Latvia*

A R T I C L E I N F O

A B S T R A C T

Antimony trisulfide (Sb_2S_3) is a promising photovoltaic absorber, which has so far been fabricated mainly by chemical deposition methods. Despite its aptness for congruent sublimation, less research efforts have been made on low-temperature Sb_2S_3 processing by physical methods. In this regard, recent studies show large variation in the processing temperature of Sb_2S_3 films, which overall brings into question the need for higher substrate temperatures (>350 °C). Furthermore, in-depth analysis of defect structure of Sb_2S_3 employing temperature-dependent admittance spectroscopy (TAS) and photoluminescence (PL) remains largely unexplored. In this work, we systematically study the effect of close-spaced sublimation (CSS) substrate temperature on Sb_2S_3 absorber growth, employing a wide temperature range of 240–400 °C. Temperatures above 320 °C caused cracking phenomena in the Sb_2S_3 absorber film, proving the unviability of higher processing temperatures. CSS processing temperature of 300 °C was found optimal, producing crack-free Sb_2S_3 films with increased presence of (hk1) planes, and achieving the best CdS/Sb_2S_3 device with photoconversion efficiency of 3.8%. TAS study revealed two deep defects with activation energies of 0.32 eV and 0.37 eV. Low-temperature PL measurement revealed a band-to-band emission at 1.72 eV and a broad band peaked at 1.40 eV, which was assigned to a donor-acceptor pair recombination. Temperature-dependent I-V analysis showed that recombination at $CdS–Sb_2S_3$ interface remains a large limitation for the device efficiency.

1. Introduction

Antimony trisulfide (Sb_2S_3) is a non-toxic and earth-abundant semiconductor material, which holds huge promise as a photovoltaic (PV) absorber for future thin film solar cell technologies. Sb_2S_3 has a suitable bandgap energy of 1.7–1.8 eV [1] and shows strong light absorption ($\alpha > 10^4$ cm^{-1}) [2]. These impressive optoelectronic properties make Sb_2S_3 feasible for applications, such as tandem solar cells [3], solar windows [4], IoT sensors [5] and water splitting devices [6,7]. Sb_2S_3 also has an orthorhombic crystal structure, with crystals growing in quasi-one-dimensional (Q1D) ribbons [2]. While ribbons are formed from Sb-S covalent bonds, ribbons only have weak van der Waals' forces between them. This has been found to have drastic effect on the charge transport across the absorber layer, with quasi-vertical, (hk1)-oriented

ribbons having been deemed optimal [8,9]. Moreover, it has led to intensive research efforts to optimize Sb_2S_3 crystal growth toward the normal of the substrate (along the [001] crystal direction, or the c-axis) [10–13].

Although Sb_2S_3 is a single-phase binary compound with a relatively low melting point (550 °C) and high vapor pressure [14], chemical methods have been preferred for the synthesis of Sb_2S_3 absorber films [4,15,16], also leading to the current state-of-the-art device efficiency of 7.5% [17]. Despite this achievement, devices deploying physically evaporated Sb_2S_3 absorbers have been recently gaining ground. Several recent studies have successfully deposited Sb_2S_3 by thermal evaporation (TE) [18,19], rapid thermal evaporation (RTE) [12,20], close-spaced sublimation (CSS) [21–23] and vapor transport deposition (VTD) [13, 24]. In these studies, a superstrate configuration was employed, with the

---

Sb_2S_3 absorber deposited onto a cadmium sulfide (CdS) buffer layer. CdS is an n-type semiconductor material that has been widely used as a heterojunction partner layer for p-type absorbers, such as CdTe, CZTS, Sb_2S_3, Sb_2Se_3 [25–28]. For instance, Lian et al. deposited Sb_2S_3 solar cells by TE and achieved photoconversion efficiency (PCE) of 6.2% [19]. Zeng et al. produced a 4.7%-efficient PV device with Sb_2S_3 absorber fabricated by VTD [24]. Xie et al. obtained PCE of 4.5% for a PV device employing a CSS-deposited Sb_2S_3 absorber [22]. A certain aspect in these studies is that rather high substrate temperatures from 350 °C to 500 °C have been used [13,22,24]. On one hand, this complies with growth conditions honed for Sb_2Se_3 solar cells, for which high processing temperatures between 450 °C and 500 °C for optimal grain growth have been reported [9,28–31]. On the other hand, lower melting point of Sb_2S_3 and higher partial pressure of sulfur (compared with selenium) indicate that high-quality material can be processed at significantly lower temperatures compared to Sb_2Se_3. Like with Sb_2Se_3, optimization of growth conditions is attributed to improved grain orientation along [001] crystal direction and increased compactness of adjacent Sb_2S_3 grains [21]. In that regard, a natural question arises whether higher processing temperatures (>350 °C) are necessary for obtaining high-quality Sb_2S_3 thin films by CSS and VTD deposition methods.

Aside from the optimization of growth conditions, another important aspect concerns the understanding of defect structure in Sb_2S_3 and recombination mechanisms at the CdS–Sb_2S_3 interface. Thus far, knowledge about the defect profile of Sb_2S_3 is often translated from works on Sb_2Se_3 devices, for which numerous deep-level transient spectroscopy (DLTS) and temperature-dependent admittance spectroscopy (TAS) studies have already been conducted [28,32,33]. However, only few studies related to deep defect analysis of Sb_2S_3 are currently available [34–36]. Moreover, low-temperature photoluminescence (PL) studies for getting a deeper insight into bulk defects in Sb_2S_3 absorber have not been successfully performed. Considering aforementioned aspects, the focus of present study is to identify suitable growth conditions for the Sb_2S_3 absorber as well as provide new insight into defects employing low-temperature PL on the Sb_2S_3 absorber and TAS on the Sb_2S_3 device.

2. Experimental

2.1. Sb_2S_3 thin-film and device fabrication

Sb_2S_3 thin film solar cells were fabricated in a superstrate configuration onto soda-lime glass substrates coated with CdS and fluorine-doped tin oxide (FTO) (20 Ω sq^{-1}) (glass/FTO/CdS/Sb_2S_3/Au). A custom-made close-spaced sublimation reactor was used to deposit CdS buffer and Sb_2S_3 absorber layers under vacuum of 10^{-4} Pa. CdS buffer layers were deposited from CdS powder (Sigma-Aldrich, 5 N) at substrate temperature of 350 °C and source temperature of 650 °C. Sb_2S_3 absorber layers were deposited from a Sb_2S_3 powder (Sigma-Aldrich, 5 N) at constant source temperature of 450 °C, while the substrate temperature was varied between 260 and 400 °C. Gold back contacts (with area of 0.25 cm^2) were evaporated on top of Sb_2S_3 absorber layers by vacuum evaporation.

2.2. Material and device characterization

X-ray diffraction (XRD) patterns were recorded using a Rigaku Ultima IV diffractometer with Cu Kα radiation (λ = 1.54 Å, 40 kV, 40 mA). Morphology and cross-sections of Sb_2S_3 films were analyzed by a Zeiss HR FESEM Ultra 55 scanning electron microscope (SEM). Raman measurements were performed with a Horiba Jobin Yvon Labram HR 800 spectrometer (λ = 532 nm). J-V curves were measured for Sb_2S_3 devices with a Wavelabs LS-2 LED solar simulator (100 mW cm^{-2}, AM1.5) in ambient air at room temperature. Temperature-dependent J-V curves were measured for the Sb_2S_3 device with a KEITHLEY 2400 SourceMeter

at temperatures 20 K–320 K with a temperature step of ΔT = 10 K. External quantum efficiency (EQE) spectra were measured with a monochromatized light source (Newport 300 W Xenon lamp, Newport Cornerstone 260 monochromator), a Merlin digital lock-in detector and a factory-calibrated Si reference detector. The ionization potential values of CdS and Sb_2S_3 layers were determined with photoelectron emission spectroscopy (PES), by using an ENERGETIQ Laser Driven Light Source (LDLS EQ-99) white light source, a Spectral Products DK240 1/4 m monochromator and a Keithley 617 electrometer. These values were later used to derive the band diagram for the whole device. For temperature-dependent admittance spectroscopy (TAS), Sb_2S_3 device was mounted on a cold finger in a closed cycle Janis helium cryostat. C-*f*-T curves were obtained using a Wayne Kerr 6500B impedance meter, where impedance, Z, and phase angle, θ, were measured at 0 V bias and 30 mV ac voltage [37]. Frequency was varied from 10 Hz to 10 MHz; temperature ranged from 20 K to 320 K. Low-temperature photoluminescence (PL) measurements were conducted using a diode-pumped Nd:YAG solid state laser with wavelength of 266 nm, pulse width of 0.6 ns, and repetition rate of 19 kHz [38]. The maximum average power was approximately 3 mW, maximum peak power density was approximately 276.5 kW cm^{-2}. PL signal was detected using a 0.5 m focal length Andor SR-500i monochromator and thermoelectrically cooled InGaAs detector IGA-030-TE2-H of Electro-Optical Systems Inc that is equipped with a Hamamatsu R632 photomultiplier tube.

3. Results and discussion

### 3.1. Structural properties of Sb_2S_3 films

Sb_2S_3 films deposited onto CdS/FTO/glass substrates by CSS at substrate temperatures ranging from 240 to 400 °C were first characterized by XRD. Fig. 1 displays XRD patterns of Sb_2S_3/CdS/FTO/glass structures (with diffractograms of CdS/FTO/glass shown separately in Fig. S1 of the Supplementary Material). Reflections at 17.5°, 22.3°, 25.0°, 28.6°, 32.6° can be assigned to orthorhombic Sb_2S_3 crystal structure with *Pbnm* space group symmetry (JCPDS 42–1393) [19]. No secondary phases were detected. The lattice parameters and crystallite size (D) were calculated for the Sb_2S_3 films and included in Table S1 of the Supplementary Material. While the lattice parameters did not show any changes related to the applied substrate temperature, the crystallite size of Sb_2S_3 grew with increasing substrate temperature. Phase composition of Sb_2S_3 films was further analyzed by Raman spectroscopy, with all spectra presented in the Supplementary Fig. S2. Regardless of the substrate temperature, Raman spectra showed identical vibrational modes corresponding to the pure Sb_2S_3 phase [39].

Sb_2S_3 crystal growth depending on the substrate temperature was investigated through texture coefficient (TC) analysis, as shown in Fig. 1b. TC values were calculated from Eq. (1):

$$TC(hkl) = \frac{I(hkl)}{I_0(hkl)} \times \left[\frac{1}{N} \sum_{i=0}^{N} \frac{I(hkl)}{I_0(hkl)} \right]^{-1} \quad (1)$$

where I(hkl) is the measured intensity for a given reflection with hkl indices, I_0(hkl) is a reference intensity for a given reflection acquired from the JCPDS Card No. 42–1393, and N is the number of reflections considered in the analysis [40].

What can be immediately noted from the calculated TC values is that Sb_2S_3 films deposited at 260 °C and 300 °C show gradually increasing TC values for 211, 221 and 501 planes, with largest TC values (exceeding 1) arising from the 501 planes. For Sb_2S_3 films deposited at 340 °C and 380 °C, the largest TC values correspond to 110 and 320 planes. It can be deduced that lower substrate temperatures help induce growth of (hk1) planes as compared to higher substrate temperatures. Previous reports on both Sb_2S_3 and Sb_2Se_3 absorbers have also deemed (hk1)-oriented crystal grains optimal for efficient charge transport across the Sb_2S_3 (Sb_2Se_3) film [12,24,41,42].
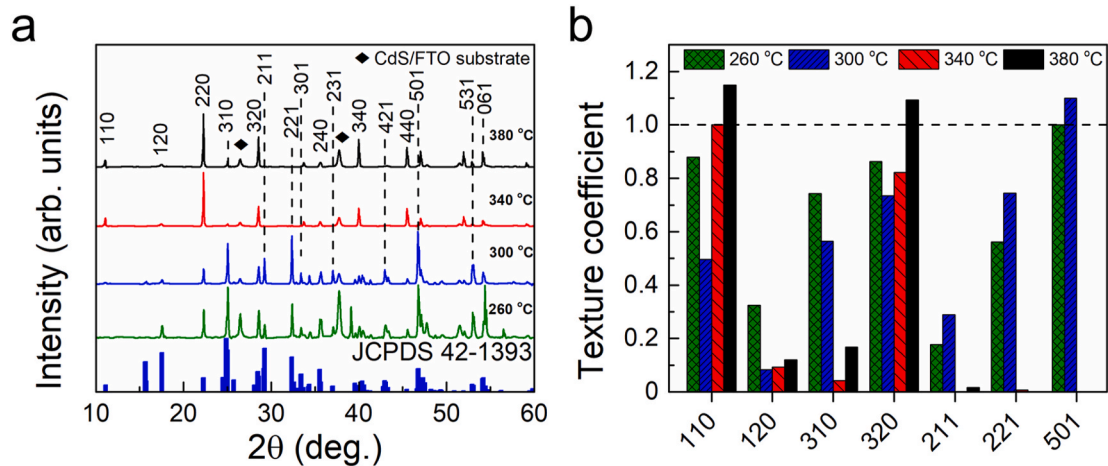
Fig. 1. (a) Sb_2S_3 absorber films deposited by CSS at substrate temperatures 260–380 °C onto CdS/FTO substrates. (b) TC values calculated from integrated intensity ratios for main crystal planes in Sb_2S_3 films.

The grain morphology in Sb_2S_3 films, deposited onto CdS/FTO/glass substrates, was analyzed by scanning electron microscopy (SEM). Top-down SEM images of Sb_2S_3 films, which were grown at substrate temperatures of 240–380 °C, as seen in Fig. 2a–d, illustrate well how the increase of substrate temperature converts to larger Sb_2S_3 grains. Ramp-up of substrate temperature caused Sb_2S_3 films to have bigger and denser plate-shaped grains as compared to smaller flakes at lower substrate temperatures (whole temperature range of 240–400 °C is shown in the Supplementary Fig. S3) – an observation that is consistent with previous CSS depositions of Sb_2Se_3 and SnS films [28,43]. Cross-sectional SEM images in Fig. 2e–h showed that Sb_2S_3 films also grow more compact with increasing substrate temperature.

While the Sb_2S_3 film fabricated at lower substrate temperature of 260 °C, as seen in Fig. 2a, shows relatively large voids between the grains, only a small number of pinholes in Fig. 2b–d are seen for Sb_2S_3 films at higher substrate temperatures. More intriguing, however, was the occurrence of microcracks, as can be clearly noted in Fig. 2d (and in Supplementary Figures S3e-h and S4a-c), which were found in Sb_2S_3 films grown at substrate temperatures of 320 °C and above. Interestingly, no cracks were noted in the previously grown Sb_2Se_3 films, also made by the CSS process [28]. It is likely that there are multiple plausible factors that altogether led to the crack formation. First, it can be argued that the cracking could be related to the difference in the thermal expansion coefficients (TECs) of orthorhombic Sb_2S_3 and Sb_2Se_3

crystals. Gan et al. reported that the TEC of Sb_2S_3 in the [010] crystal direction is two to seven times larger than the TECs in the [100] and [001] crystal direction [44]. At the same time, Herrmann et al. showed that Sb_2Se_3 has nearly identical TECs values in all three crystal directions [45]. This implies that Sb_2S_3 films could be subject to greater residual stress during the deposition process at higher temperatures. If there is either substantial tensile or compressive stress within the film, it could lead to crack formation [46,47]. Second, since Sb_2S_3 has a lower melting point (550 °C) compared with Sb_2Se_3 (611 °C) [9], it exhibits higher vapor pressure and sublimation is expected at lower temperatures. Therefore, substrate temperatures from 320 °C onwards could have induced such an intense re-sublimation of the already deposited Sb_2S_3 film, which eventually led to the crack formation in the Sb_2S_3 films.

### 3.2. Sb_2S_3 device properties depending on the CSS substrate temperature

Having noted systematic structural changes in the Sb_2S_3 film growth, the impact of CSS deposition temperature on the performance of superstrate glass/FTO/CdS/Sb_2S_3/Au solar cells was subsequently investigated. Fig. 3a–d shows main photovoltaic parameters with average values for devices with Sb_2S_3 deposited at substrate temperatures of 240–400 °C. Illuminated current density–voltage (J–V) curves are shown in Fig. 4a for the best devices. As seen in Fig. 3a–d, two
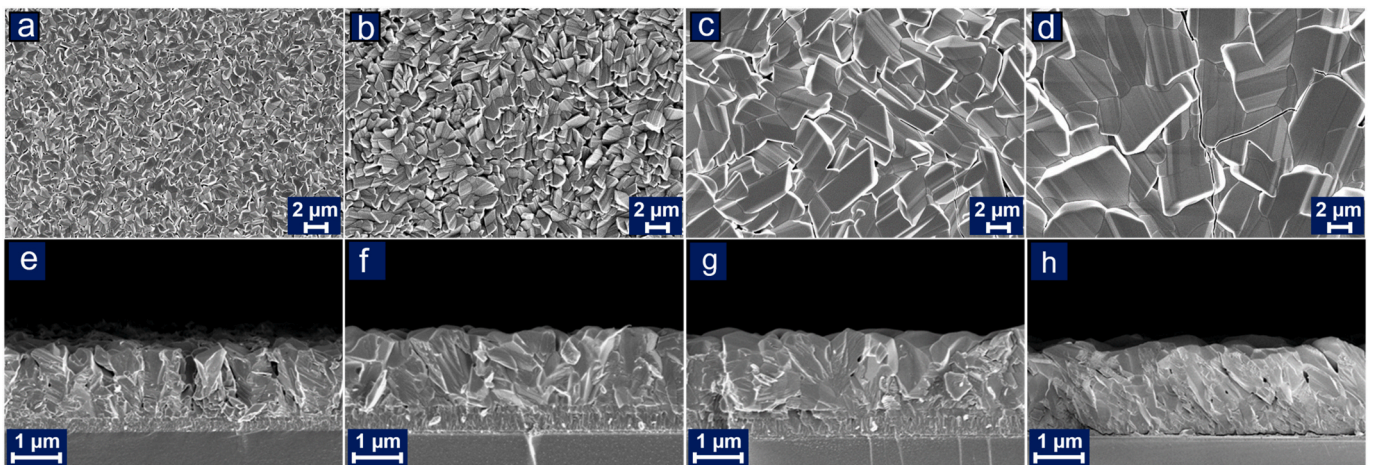
Fig. 2. Top-down (a–d) and cross-sectional (e–h) SEM images of Sb_2S_3 absorber films, which are deposited at varying substrate temperatures of 260 °C (a, e), 300 °C (b, f), 340 °C (c, g), and 380 °C (d, h) onto CdS/FTO/glass substrates.
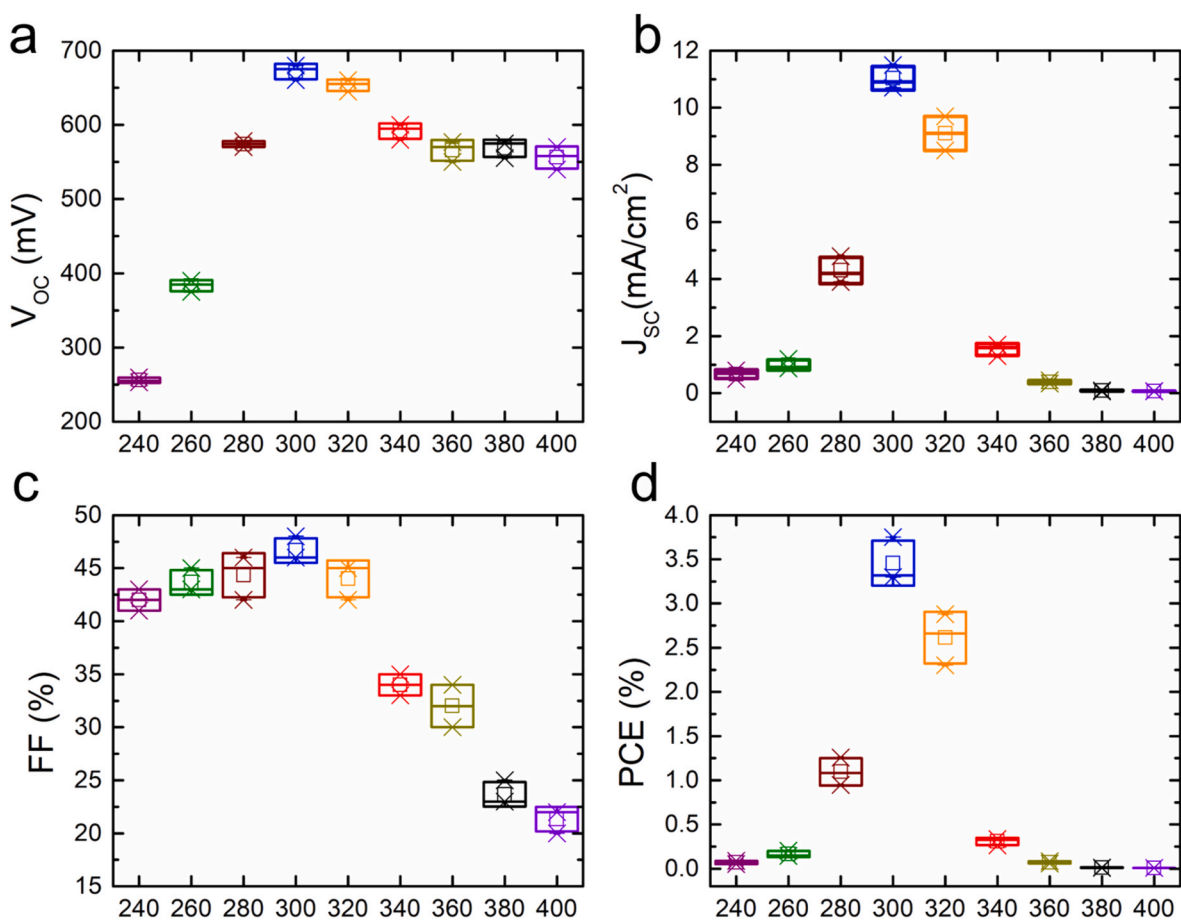
Fig. 3. Main photovoltaic parameters including (a) open circuit voltage (V_{OC}), (b) short circuit current density (J_{SC}), (c) fill factor (FF) and (d) photoconversion efficiency (PCE) with average values (marked as hollow squares) measured for Sb_2S_3 devices with Sb_2S_3 absorber deposited at substrate temperatures in the range of 240–400 °C.
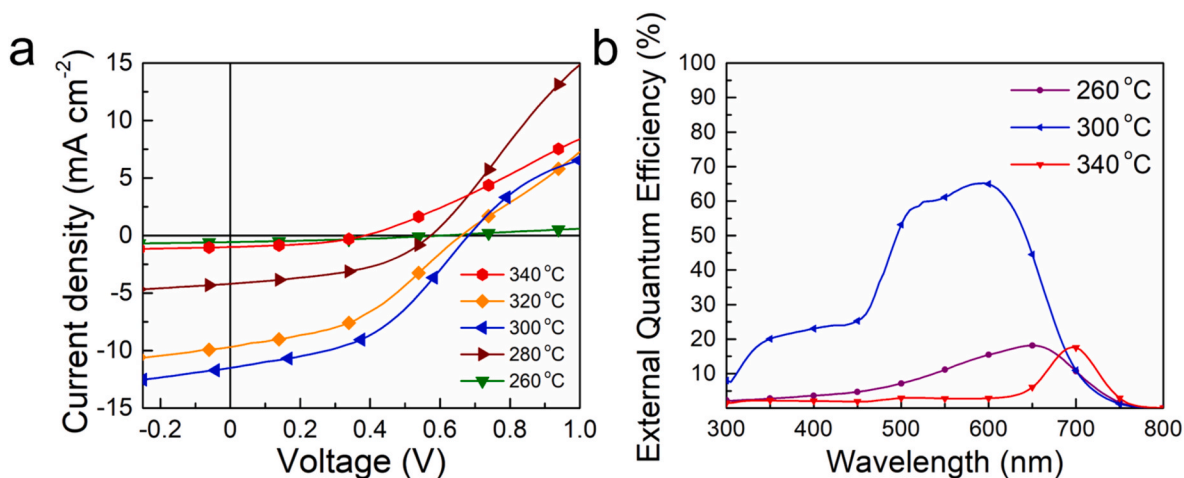
Fig. 4. (a) Illuminated J–V curves of best Sb_2S_3 devices and (b) external quantum efficiency (EQE) plots of Sb_2S_3 devices with Sb_2S_3 absorber layer deposited at substrate temperatures of 260–340 °C.

distinct regions can be noted. In the first region, from 240 °C to 300 °C, there is a gradual increase of all PV parameters, including open- circuit voltage (V_{OC}), current density (J_{SC}), fill factor (FF), and PCE. The maximum PV parameters, namely J_{SC} of 11.5 mA cm^{-2}, V_{OC} of 680 mV, FF of 48%, and PCE of 3.8% were obtained for the substrate temperature of 300 °C. In the second region, starting from substrate temperature of 320 °C, all the PV parameters start to decline. Interestingly, while the

V_{OC} shows only a slight decrease before plateauing at 550 mV, both J_{SC} and FF undergo a significant drop, with J_{SC} reducing to microamperes.

External quantum efficiency (EQE) measurements, as seen in Fig. 4b, support the trend observed during the J–V measurements, with the best device showing highest EQE response for the whole wavelength region. The band gap energy of ~1.8 eV was determined for the best Sb_2S_3 device (Supplementary Fig. S5). Nevertheless, the best device suffers a

significant EQE response drop in the short wavelength region, which is associated with parasitic absorption in the CdS buffer layer [28]. Such absorption has been widely reported also in CdTe and Sb_2Se_3 cells, where a CdS buffer was employed [48,49]. For all the devices obtained with Sb_2S_3 deposited at temperatures higher than 340 °C, there was a futile EQE response throughout the whole wavelength region. This can be attributed to the detected microcracks, which were seen in the top-down and cross-sectional SEM images (Supplementary Figs. S4a–c), and which inherently lead to the current leakage, further evidenced by low FF values shown in Fig. 3c.

Based on the cumulative structural analysis of Sb_2S_3 absorber films and device characterization of respective Sb_2S_3 solar cells, it was demonstrated that the optimal CSS deposition of Sb_2S_3 films takes place at a substrate temperature of 300 °C, where a compact Sb_2S_3 grain growth is achieved together with increased presence of favorable (hk1) planes. When compared with recent reports on the Sb_2S_3 fabrication with CSS and VTD techniques, the optimal processing temperature found in the current work is clearly lower than the deposition temperature interval of 350–450 °C reported elsewhere [13,22,24]. For instance, Hiu et al., reported a VTD deposition temperature of 495 °C for depositing Sb_2S_3 films, and achieved a PCE of 4.7% for the superstrate glass/ITO/CdS/Sb_2S_3/Au device [24]. Zeng et al., reported a 1.4%-efficient CdS/Sb_2S_3 device, where a higher CSS processing temperature (no exact values were given) was found optimal for high-quality Sb_2S_3 absorber [23]. Employing a similar CSS deposition technique, although with an additional selenization process, Xie et al., produced a device with PCE of 4.5% [13]. In this work, the optimal source and substrate temperatures in the CSS reactor were 450 °C and 370 °C, respectively [13]. Guo et al., used an identical CSS technique and obtained a device efficiency of 3.8% after screening substrate temperatures of 300–400 °C [21]. However, for the best Sb_2S_3 device, optimal substrate temperature was not provided. When looking at

studies where TE method was used, e.g., Chen et al., similarly found optimal substrate temperatures being in the 300–320 °C range, with the device achieving PCE of 3.0% [18]. Lian et al., followed a similar approach, employing a substrate temperature of 300 °C, yet also including a selenization step for the Sb_2S_3 absorber and a spiro-OMeTAD hole transport material (HTM) atop the absorber, which yielded a device with PCE of 6.2% [19]. As can be seen, the latter findings reported substrate temperatures that match well with the results obtained in this study. In addition, we revealed a physical phenomenon that had not been reported before. It is important to emphasize that the cracking phenomenon of Sb_2S_3 films, observed during the CSS deposition at temperatures 340–400 °C, had a clear impact on the eventual solar cell performance. Had the cracking phenomena not occurred, then inferring from previous experience with the CSS deposition of CdTe and Sb_2Se_3 [28,50], e.g., Sb_2S_3 films grown at higher substrate temperatures, such as seen in Fig. 2c and d, would have probably performed better, given that the films have larger grains and higher level of compactness. Although cracking might be an expected occurrence at elevated temperatures in thin film technologies, it was still unusual for an antimony chalcogenide material, and it could have direct implications for some of the proposed applications. For instance, such physical phenomena could mean Sb_2S_3 is not compatible as a bottom cell for the recently proposed Sb_2Se_3–Sb_2S_3 monolithic tandem solar cell [3].

3.3. Factors limiting the Sb_2S_3 device performance

Temperature-dependent J–V (J–V–T) curves, as shown in Fig. 5a, were measured to acquire better understanding of potential recombination processes for the best CdS/Sb_2S_3 device (PCE = 3.8%). Fig. 5b shows a derived plot of logarithm of series resistance, R_S, vs. 1000/T, where R_S increases with decreasing temperatures. Such behavior can be attributed to trapping of free carriers in the Sb_2S_3 bulk, which
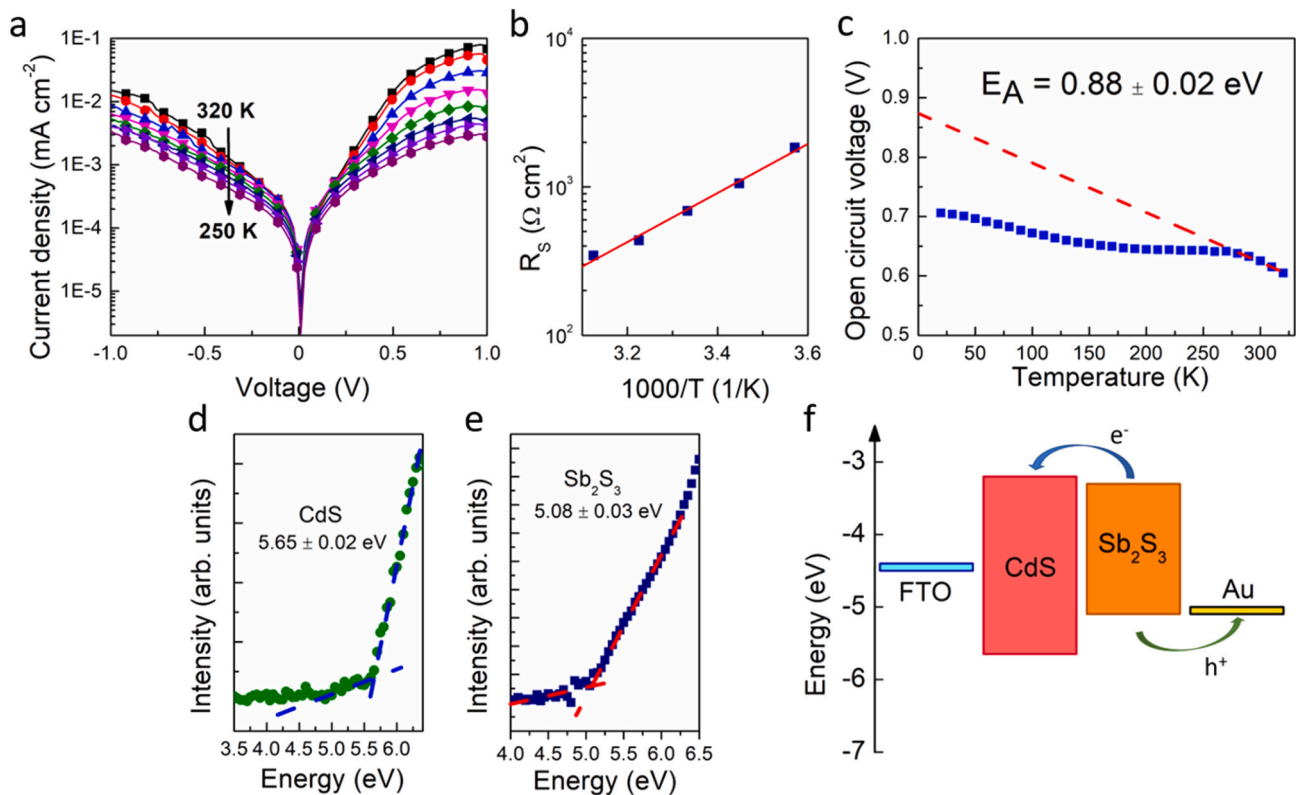
Fig. 5. (a) Semi-log plot of dark J–V curves, (b) series resistance derived from dark J–V curves plotted against 1000/T, (c) activation energy calculated from the open-circuit voltage vs. T (V_{OC}–T) plot, photoelectron emission spectroscopy (PES) spectra of (d) CdS on FTO/glass substrate and (e) Sb_2S_3 on CdS/FTO/glass substrates, (f) derived band diagram for the FTO/CdS/Sb_2S_3/Au solar cell structure (CdS band gap value taken from [53]).

contributes to a significant R_S increase at lower temperatures [51]. The dominant recombination process in the CdS–Sb$_2$S$_3$ heterojunction was determined from the plot of temperature dependence of open-circuit voltage (V$_{OC}$–T), as shown in Fig. 5c. Activation energy, E$_A$, for the recombination process was found according to Eq. (2)

$$V_{OC} = \frac{E_A}{q} - \frac{Ak_BT}{q} \ln\left(\frac{J_{00}}{J_L}\right) \qquad (2)$$

where E_A is the activation energy of the predominant recombination process, q is the elementary charge, A is the ideality factor, k$_B$ is the Boltzmann constant, T is temperature, J_{00} is the reference current density and J_L is the photocurrent density [51].

Linear extrapolation from higher temperatures to 0 K in the V$_{OC}$–T plot gave the activation energy of 0.88 ± 0.02 eV, which is much lower than the Sb$_2$S$_3$ band gap energy of 1.8 eV. This implies that interface recombination is the dominant recombination process in the CdS/Sb$_2$S$_3$ device. In addition, photoelectron emission spectroscopy (PES) was performed on CdS and Sb$_2$Se$_3$ films, as shown in Fig. 5d and e, respectively, to elucidate band alignment for the FTO/CdS/Sb$_2$S$_3$/Au device structure. Ionization potential (I$_p$) was found through extrapolation of the linear fit from valence band edge photoemission to 0 eV, giving ionization potentials of 5.65 ± 0.02 eV and 5.08 ± 0.03 eV for CdS and Sb$_2$S$_3$, respectively. Considering the band gap values of CdS and Sb$_2$S$_3$, a band diagram of the device was subsequently drawn, as shown in Fig. 5f, which revealed a small positive conduction band offset (CBO) of ≈0.1 eV between the CdS buffer and Sb$_2$S$_3$ absorber. Although it implies a formation of a spike, an electrostatic barrier to electrons moving to the front electrode, it has been argued that for such a small CBO, thermionic emission across the junction would still allow unimpeded charge transport [52,53].

Deep defects could also explain substantial V$_{OC}$ losses in the CdS/Sb$_2$S$_3$ devices. TAS enables characterization of deep defects in the Sb$_2$S$_3$ absorber, where the overall capacitance response has contribution from free carriers, bulk defects, and interface defects [41]. Impedance, Z (ω, T), and phase angle, θ (ω, T), were measured to calculate capacitance, C, using an equivalent circuit model, which includes a capacitor, a series resistor, and a parallel resistor [10,37]. In the case of a capacitance step, its relaxation frequency, ω_0, was found from the maxima of a derivative capacitance ($-\omega dC/d\omega$) plot. In the Arrhenius plot, natural logarithms of relaxation frequencies were plotted against inverse temperature to calculate the activation energy, E$_A$, and thermal emission prefactor, ξ_0, according to Eq. (2) [37,54]:

$$\omega_0 = 2\pi f_0 = 2\xi_0 T^2 \exp\left(-E_A / k_B T\right) \qquad (3)$$

where ξ_0 is the thermal emission prefactor, k_B is Boltzmann constant, T is temperature and E_A is the activation energy of defect level.

Temperature–dependent capacitance–frequency (C-f-T) curves of a Sb$_2$S$_3$ device are shown in Fig. 6a. From the derivative capacitance plot,

as shown in Fig. 6b, two distinct maxima could be discerned. Fig. 6c shows the Arrhenius plot with two activation energies: E$_{A1}$ of 0.32 eV (ξ_0 of 4.2 × 10^6 s^{-1} K^{-2}) and E$_{A2}$ of 0.37 eV (ξ_0 of 5.2 × 10^6 s^{-1} K^{-2}). The activation energy of 0.32 eV has also been reported in a DLTS study on a TiO$_2$/Sb$_2$S$_3$ solar cell and was assigned to an Sb vacancy (V$_{Sb}$) [55]. A first-principles calculations study assigned comparable activation energies to a S antisite (S$_{Sb}$) defect and an Sb vacancy, respectively, and where both were reported to exist in high concentration due to low formation energy [56]. Furthermore, a DFT study on intrinsic Sb$_2$S$_3$ found that V$_{Sb}$ defects have two ionization energies between 0.3 and 0.4 eV, although these defects show relatively high defect formation energies [21]. Based on these reports and prior admittance measurements on the Sb$_2$Se$_3$ counterpart [10], at least one of the activation energies could be ascribed to the Sb vacancy.

Fig. 7 shows PL spectra measured at 3–70 K for the Sb$_2$S$_3$ deposited at substrate temperature of 300 °C onto the CdS/FTO/glass substrate. It is important to mention that initial PL measurements were performed using a continuous wave He-Cd gas laser and an InGaAs detector [43, 57]. Since the continuous wave laser led to localized heating of the sample and given that a half-band was detected at around 1.35 eV, which was at the detection limit of the working range of the InGaAs photomultiplier tube (0.77–1.35 eV), a pulsed laser with a detection limit greater than 1.35 eV was opted. Fig. 7a shows PL spectra that revealed two PL bands: a narrow emission band peaked at 1.72 eV and a very broad asymmetric emission band peaked at around 1.40 eV.

The band D1 peaked at 1.72 eV was fitted by assuming there is a single peak and is related to a band-to-band transition. The broad band D2 was fitted by a single asymmetric sigmoidal function for the deconvolution of asymmetric band, as presented in Fig. 7b [38,57]. Thereby, we obtained temperature-dependent PL spectra of band D2, as shown in Fig. 7c, which peak at approximately 1.40 eV. It is worth mentioning that while D1 band-to-band transition has been reported by a recent study employing room-temperature PL, to the best of our knowledge, the D2 band-related emission has not been reported thus far. To gain better understanding of the peculiarity of this band, the Arrhenius plot, as shown in Fig. 7d, was derived to calculate thermal activation energy, E$_A$, of the D2 band. Activation energy of 10 ± 2 meV was obtained, indicating that at least one shallow defect is involved in that recombination. In a classical approach, laser power dependence can provide supporting evidence if this D2 band originates from a donor-acceptor-pair (DAP) recombination. However, since at higher laser power (≥10 mW) sample degradation was observed, and at lower laser power (<3 mW) intensity of the signal was lost, we were not able to conduct laser power dependence measurements. Nevertheless, a subtle blue shift of the D2 band was observed with increasing temperature. Such a phenomenon, where a band is shifted toward higher energies with increasing temperature, has been related to a DAP recombination at low temperatures [43]. To satisfy this DAP mechanism, we should assume contribution from a certain deep donor defect, such as the S
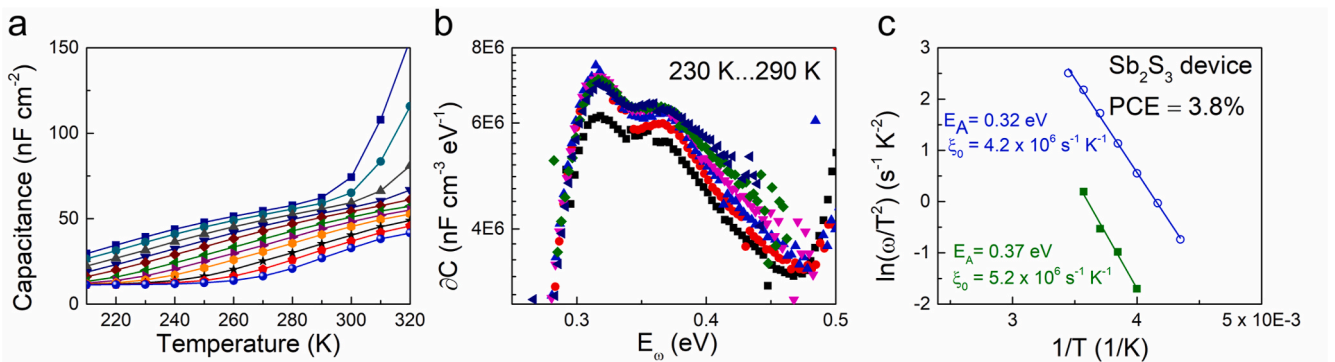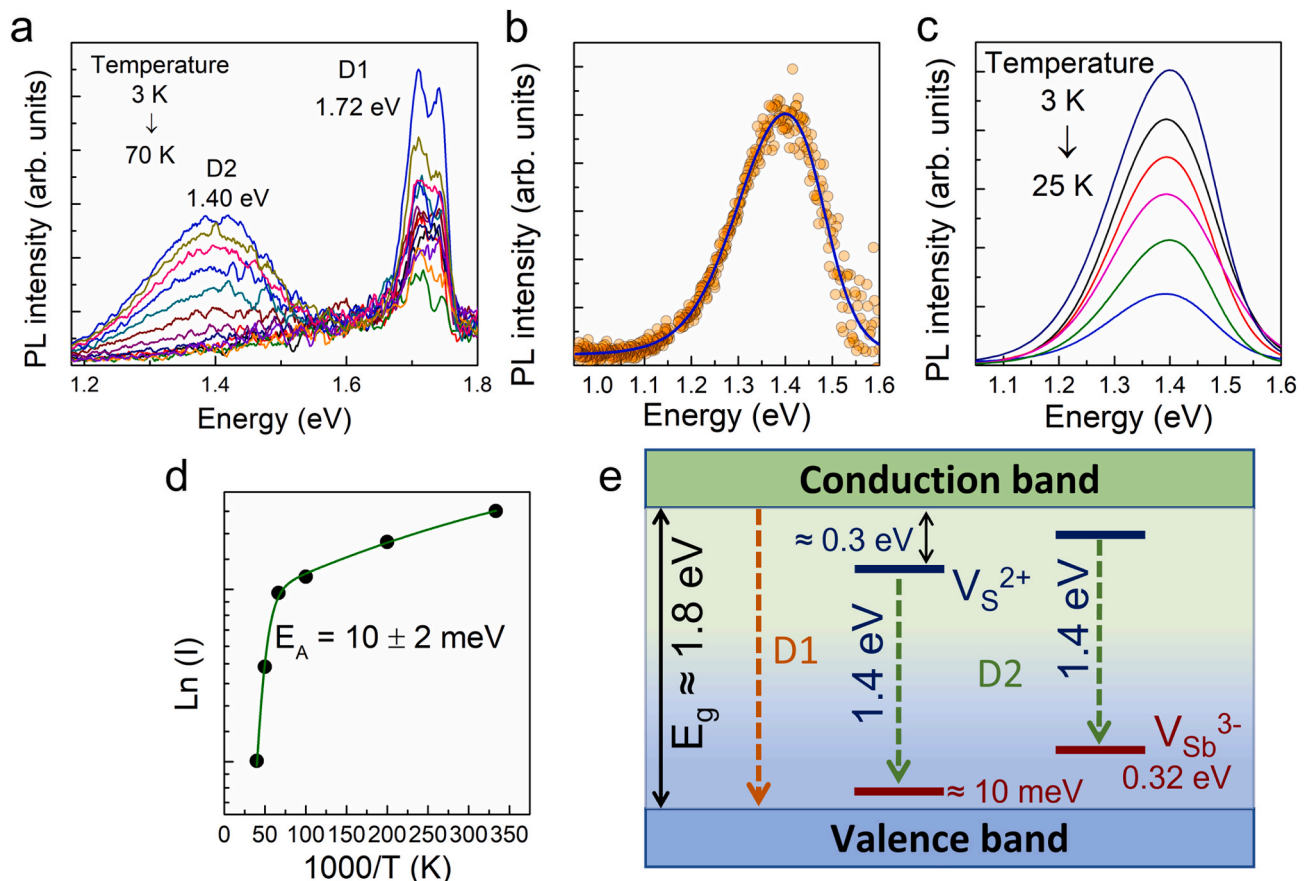

Fig. 6. (a) C-f-T curves of CdS/Sb$_2$S$_3$ solar cell (PCE = 3.8%) measured from 80 to 320 K, (b) $-\omega dC(\omega)/d\omega$ vs E$_\omega$ plots that show two distinct peaks, (c) Arrhenius plot of ln (ω/T^2) vs. 1/T used to calculate activation energies and thermal emission prefactors.

Fig. 7. (a) Low-temperature PL spectra of Sb_2S_3 films deposited at substrate temperature of 300 °C onto a CdS/FTO/glass substrate. For the given sample, (b) fitting of an asymmetric D2 band by using a single asymmetric sigmoidal function, and (c) temperature-dependent fitted PL spectra of D2 band measured in the temperature range of 3–25 K (d) Arrhenius plot giving thermal activation energy of the D2 band in Sb_2S_3, which was obtained from fitted PL spectra, (e) model visualizing D1 band-to-band emission and D2 emission originating from a deep donor to shallow acceptor transition and/or from a deep donor to deep acceptor (V_{Sb}) transition.

vacancy (V_S) (0.3–0.6 eV) [55,56]. According to this scenario, the donor level will be occupied provided the temperature is increased, and recombination occurs between the conduction band and a deep acceptor. According to TAS results, this deep acceptor can be assigned to the Sb vacancy (V_{Sb}). As a rule of thumb, there is always one type of disorder, which prevails over others in the crystal lattice. Given that the theoretical studies have provided low formation energies for vacancy defects (V_{Sb}, V_S) [55,56], we consider these Schottky defects to be pre-dominant and provide their formation mechanism in the Supplementary Material. Based on the above discussion and existence of possible defect levels, a DAP model is proposed in Fig. 7e. For the given model, it can be assumed the DAP transition could be related to either the transition between deep donor (DD) to shallow acceptor transition and/or between deep donor (V_S) and deep acceptor (V_{Sb}, as determined from TAS measurements). For better clarification, laser power dependence measurements would be needed to ascertain the shift of the band peak position per decade. Nevertheless, the presence of such complex defects is detrimental to the performance of Sb_2S_3 device, potentially limiting the built-in voltage and photocurrent collection.

4. Conclusions

In conclusion, we systematically studied the effect of substrate temperature on the Sb_2S_3 absorber growth with the CSS method, employing a wide substrate temperature range of 240–400 °C. It was found that CSS processing temperature of 300 °C is optimal, resulting in compact crack-free films with increased presence of favorable (hk1) planes. Higher substrate temperatures (340–380 °C) caused Sb_2S_3 films

to have bigger, more dense plate-shaped grains as compared to smaller flakes at lower substrate temperatures (240–280 °C), However, micro-cracks were detected in Sb_2S_3 films starting from substrate temperature of 320 °C. The maximum PV parameters, namely J_{SC} of 11.5 mA cm^{-2}, V_{OC} of 680 mV, FF of 48%, and PCE of 3.8% were obtained for the substrate temperature of 300 °C. For the same device the EQE showed the best response over the entire 300–800 nm wavelength range. For the best device, extraction of activation energy from the V_{OC}–T plot indicated that interface recombination is the dominant recombination mechanism in these devices. Based on the determined ionization potentials, a band diagram was derived, which showed favorable band alignment between the CdS buffer and Sb_2S_3 absorber. TAS study showed two deep defects with activation energies of 0.32 eV and 0.37 eV, while low-temperature PL measurement revealed a band-to-band emission at 1.72 eV and a broad band peaked at 1.40 eV, which was assigned to a donor-acceptor pair recombination. Although the device efficiency of 3.8% is a promising achievement and well-placed result within reported Sb_2S_3 based devices processed by physical deposition methods, the limitation factors like absorber-buffer interface recombination and existence of deep defects in the absorber remain the key issues for this device structure. Further technological steps, such as post-deposition treatments and doping, combined with in-depth advanced characterization, need to be implemented to progress the development of emerging cost-efficient and environmentally friendly Sb_2S_3 thin-film solar cells.

CRediT authorship contribution statement

R. Krautmann: Writing – original draft, Visualization, Validation, Methodology, Investigation, Formal analysis, Data curation, Conceptualization. **N. Spalatu:** Writing – review & editing, Visualization, Validation, Supervision, Methodology, Investigation, Funding acquisition, Formal analysis, Conceptualization. **R. Josepson:** Visualization, Formal analysis. **R. Nedzinskas:** Visualization, Validation, Formal analysis. **R. Kondrotas:** Visualization, Validation, Formal analysis. **R. Grzibovskis:** Visualization, Validation, Formal analysis. **A. Vembris:** Visualization, Validation, Formal analysis. **M. Krunks:** Visualization, Validation, Project administration, Funding acquisition, Formal analysis. **I. Oja Acik:** Validation, Supervision, Project administration, Funding acquisition, Formal analysis.

Declaration of competing interest

The authors declare that they have no known competing financial interests or personal relationships that could have appeared to influence the work reported in this paper.

Data availability

No data was used for the research described in the article.

Acknowledgments

Appendix B. Supplementary data

Supplementary data to this article can be found online at https://doi.org/10.1016/j.solmat.2022.112139.

References

[1] M.Y. Versavel, J.A. Haber, Structural and optical properties of amorphous and crystalline antimony sulfide thin-films, Thin Solid Films 515 (2007) 7171–7176, https://doi.org/10.1016/J.TSF.2007.03.043.
[2] R. Kondrotas, C. Chen, J. Tang, Sb2S3 solar cells, Joule 2 (2018) 857–878, https://doi.org/10.1016/J.JOULE.2018.04.003.
[3] Y. Cao, X. Zhu, J. Jiang, C. Liu, J. Zhou, J. Ni, J. Zhang, J. Pang, Rotational design of charge carrier transport layers for optimal antimony trisulfide solar cells and its integration in tandem devices, Sol. Energy Mater. Sol. Cell. 206 (2020), 110279, https://doi.org/10.1016/J.SOLMAT.2019.110279.
[4] J.S. Eensalu, A. Katerski, E. Kärber, L. Weinhardt, M. Blum, C. Heske, W. Yang, I. O. Acik, M. Krunks, Semitransparent Sb2S3 thin film solar cells by ultrasonic spray pyrolysis for use in solar windows, Beilstein J. Nanotechnol. 10 (2019) 2396–2409, https://doi.org/10.3762/BJNANO.10.230, 230. 10.
[5] K. Li, F. Li, C. Chen, P. Jiang, S. Lu, S. Wang, Y. Lu, G. Tu, J. Guo, L. Shui, Z. Liu, B. Song, J. Tang, One-dimensional Sb2Se3 enabling ultra-flexible solar cells and mini-modules for IoT applications, Nano Energy 86 (2021), 106101, https://doi.org/10.1016/J.NANOEN.2021.106101.
[6] L. Wang, W. Lian, B. Liu, H. Lv, Y. Zhang, X. Wu, T. Wang, J. Gong, T. Chen, H. Xu, L. Wang, Y. Zhang, H. Xu, W. Lian, H. Lv, X. Wu, T. Chen, B. Liu, T. Wang, J. Gong, A transparent, high-performance, and stable Sb2S3 photoanode enabled by heterojunction engineering with conjugated polycarbazole frameworks for unbiased photoelectrochemical overall water splitting devices, Adv. Mater. 34 (2022), 2200723, https://doi.org/10.1002/ADMA.202200723.
[7] Z. Zafar, S. Yi, J. Li, C. Li, Y. Zhu, A. Zada, W. Yao, Z. Liu, X. Yue, Recent development in defects engineered photocatalysts: an overview of the experimental and theoretical strategies, Energy & Environmental Materials 5 (2022) 68–114, https://doi.org/10.1002/EEM2.12171.
[8] L. Wang, D.B. Li, K. Li, C. Chen, H.X. Deng, L. Gao, Y. Zhao, F. Jiang, L. Li, F. Huang, Y. He, H. Song, G. Niu, J. Tang, Stable 6%-efficient Sb2Se3 solar cells with a ZnO buffer layer, Nat. Energy 2 (2017), 17046, https://doi.org/10.1038/nenergy.2017.46.
[9] T.D.C. Hobson, L.J. Phillips, O.S. Hutter, H. Shiel, J.E.N. Swallow, C.N. Savory, P. K. Nayak, S. Mariotti, B. Das, L. Bowen, L.A.H. Jones, T.J. Featherstone, M. J. Smiles, M.A. Farnworth, G. Zoppi, P.K. Thakur, T.-L. Lee, H.J. Snaith, C. Leighton, D.O. Scanlon, V.R. Dhanak, K. Durose, T.D. Veal, J.D. Major, Isotype heterojunction solar cells using n-type Sb2Se3 thin films, Chem. Mater. (2020), https://doi.org/10.1021/acs.chemmater.0c00223.
[10] R. Krautmann, N. Spalatu, R. Gunder, D. Abou-Ras, T. Unold, S. Schorr, M. Krunks, I. Oja Acik, Analysis of grain orientation and defects in Sb2Se3 solar cells fabricated by close-spaced sublimation, Sol. Energy 225 (2021) 494–500, https://doi.org/10.1016/J.SOLENER.2021.07.022.
[11] X. Jin, Y. Fang, T. Salim, M. Feng, S. Hadke, S. Woei Leow, T. Chien Sum, L. H. Wong, X. Jin, Y. Fang, T. Salim, S. Hadke, S.W. Leow, L.H. Wong, M. Feng, T. C. Sum, In situ growth of [hk1]-Oriented Sb2S3 for solution-processed planar heterojunction solar cell with 6.4% efficiency, Adv. Funct. Mater. 30 (2020), 2002887, https://doi.org/10.1002/ADFM.202002887.
[12] S. Yuan, H. Deng, D. Dong, X. Yang, K. Qiao, C. Hu, H. Song, H. Song, Z. He, J. Tang, Efficient planar antimony sulfide thin film photovoltaics with large grain and preferential growth, Sol. Energy Mater. Sol. Cell. 157 (2016) 887–893, https://doi.org/10.1016/J.SOLMAT.2016.07.050.
[13] H. Zhang, S. Yuan, H. Deng, M. Ishaq, X. Yang, T. Hou, U.A. Shah, H. Song, J. Tang, Controllable orientations for Sb2S3 solar cells by vertical VTD method, Prog. Photovoltaics Res. Appl. 28 (2020) 823–832, https://doi.org/10.1002/PIP.3278.
[14] K. Wang, J. Cheng, X. Yang, R. Hu, L. Fu, J. Huang, J. Yu, L. Li, Enhanced photovoltaic properties in Sb2S3 planar heterojunction solar cell with a fast selenylation approach, Nanoscale Res. Lett. 13 (2018) 1–7, https://doi.org/10.1186/S11671-018-2651-X/TABLES/3.
[15] N. Juneja, S. Mandati, A. Katerski, N. Spalatu, S. Daskeviciute-Geguziene, A. Vembris, S. Karazhanov, V. Getautis, M. Krunks, I. Oja Acik, Sb2S3 solar cells with a cost-effective and dopant-free fluorene-based enamine as a hole transport material, Sustain. Energy Fuels 6 (2022) 3220–3229, https://doi.org/10.1039/D2SE00356B.
[16] P. Büttner, F. Scheler, D. Döhler, M.K.S. Barr, M. Bosch, M. Rey, T. Yokosawa, S. Hinz, J. Maultzsch, E. Spiecker, N. Vogel, I. Mínguez-Bacho, J. Bachmann, Continuous, crystalline Sb2S3 ultrathin light absorber coatings in solar cells based on photonic concentric p-i-n heterojunctions, Nano Energy 103 (2022), 107820, https://doi.org/10.1016/J.NANOEN.2022.107820.
[17] Y.C. Choi, D.U. Lee, J.H. Noh, E.K. Kim, S. il Seok, Highly improved Sb2S3 sensitized-inorganic-organic heterojunction solar cells and quantification of traps by deep-level transient spectroscopy, Adv. Funct. Mater. 24 (2014) 3587–3592, https://doi.org/10.1002/ADFM.201304238.
[18] X. Chen, Z. Li, H. Zhu, Y. Wang, B. Liang, J. Chen, Y. Xu, Y. Mai, CdS/Sb2S3 heterojunction thin film solar cells with a thermally evaporated absorber, J Mater Chem C Mater 5 (2017) 9421–9428, https://doi.org/10.1039/C7TC02460F.
[19] W. Lian, C. Jiang, Y. Yin, R. Tang, G. Li, L. Zhang, B. Che, T. Chen, Revealing composition and structure dependent deep-level defect in antimony trisulfide photovoltaics, Nature Communications 2021 12 (2021) 1–7, https://doi.org/10.1038/s41467-021-23592-0, 1. 12.
[20] S. Yuan, H. Deng, X. Yang, C. Hu, J. Khan, W. Ye, J. Tang, H. Song, Postsurface selenization for high performance Sb2S3 planar thin film solar cells, ACS Photonics 4 (2017) 2862–2870, https://doi.org/10.1021/ACSPHOTONICS.7B00858/ASSET/IMAGES/LARGE/PH-2017-00858S_0008 (JPEG).
[21] L. Guo, B. Zhang, S. Li, Q. Zhang, M. Buettner, L. Li, X. Qian, F. Yan, Scalable and efficient Sb2S3 thin-film solar cells fabricated by close space sublimation, Apl. Mater. 7 (2019), 041105, https://doi.org/10.1063/1.5090773.
[22] Y. Xie, K. Li, X. Li, F. Gao, X. Xiong, G. Zeng, B. Li, Fabrication of Sb2S3 solar cells by close space sublimation and enhancing the efficiency via co-selenization, Mater. Sci. Semicond. Process. 142 (2022), 106451, https://doi.org/10.1016/J.MSSP.2022.106451.
[23] Y. Zeng, F. Liu, X. Hao, Fabrication of Sb 2 S 3 planar thin film solar cells with closed-space sublimation method, 2018 IEEE 7th World Conference on Photovoltaic Energy Conversion, in: WCPEC 2018 - A Joint Conference of 45th IEEE PVSC, 28th PVSEC and 34th EU PVSEC, 2018, pp. 870–872, https://doi.org/10.1109/PVSC.2018.8547305.
[24] Y. Zeng, K. Sun, J. Huang, M.P. Nielsen, F. Ji, C. Sha, S. Yuan, X. Zhang, C. Yan, X. Liu, H. Deng, Y. Lai, J. Seidel, N. Ekins-Daukes, F. Liu, H. Song, M. Green, X. Hao, Quasi-vertically-orientated antimony sulfide inorganic thin-film solar cells achieved by vapor transport deposition, ACS Appl. Mater. Interfaces 12 (2020) 22825–22834, https://doi.org/10.1021/ACSAMI.0C02697/ASSET/IMAGES/LARGE/AM0C02697_0006 (JPEG).
[25] T.P. Shalvey, H. Shiel, O.S. Hutter, G. Zoppi, L. Bowen, V.R. Dhanak, J.D. Major, Sodium fluoride doping approach to CdTe solar cells, ACS Appl. Energy Mater. 5 (2022) 3888–3897, https://doi.org/10.1021/ACSAEM.1C03351/ASSET/IMAGES/LARGE/AE1C03351_0007 (JPEG).
[26] M. Valdes, A. Hernandez, Y. Sánchez, R. Fonoll, M. Placidi, V. Izquierdo, A. Cabas-Vidani, M. Valentini, A. Mittiga, P. Pistor, C. Malerba, E. Saucedo, A new approach for alkali incorporation in Cu2ZnSnS4 solar cells, J. Phys.: Energy 4 (2022), 044008, https://doi.org/10.1088/2515-7655/AC96A4.

[27] T.P. Weiss, I. Minguez-Bacho, E. Zuccalà, M. Melchiorre, N. Valle, E. Adib Brahime, Yokosawa Tadahiro, Erdmann Spiecker, J. Bachmann, P.J. Dale, S. Siebentritt, Post-deposition annealing and interfacial atomic layer deposition buffer layers of Sb2Se3/CdS stacks for reduced interface recombination and increased open-circuit voltages, Prog. Photovoltaics Res. Appl. (2022), https://doi.org/10.1002/PIP.3625.

[28] N. Spalatu, R. Krautmann, A. Katerski, E. Karber, R. Josepson, J. Hiie, I.O. Acik, M. Krunks, Screening and optimization of processing temperature for Sb2Se3 thin film growth protocol: interrelation between grain structure, interface intermixing and solar cell performance, Sol. Energy Mater. Sol. Cell. 225 (2021), 111045, https://doi.org/10.1016/j.solmat.2021.111045.

[29] V. Kumar, E. Artegiani, A. Kumar, G. Mariotto, F. Piccinelli, A. Romeo, Effects of post-deposition annealing and copper inclusion in superstrate Sb2Se3 based solar cells by thermal evaporation, Sol. Energy 193 (2019) 452–457, https://doi.org/10.1016/j.solener.2019.09.069.

[30] K.J. Tiwari, M. Neuschitzer, M. Espíndola-Rodriguez, Y. Sánchez, Z. Jehl, P. Vidal-Fuentes, E. Saucedo, P. Malar, Efficient Sb2Se3/CdS planar heterojunction solar cells in substrate configuration with (hk0) oriented Sb2Se3 thin films, Sol. Energy Mater. Sol. Cell. 215 (2020), 110603, https://doi.org/10.1016/j.solmat.2020.110603.

[31] I. Caño, P. Vidal-Fuentes, L. Calvo-Barrio, X. Alcobé, J.M. Asensi, S. Giraldo, Y. Sánchez, Z. Jehl, M. Placidi, J. Puigdollers, V. Izquierdo-Roca, E. Saucedo, Does Sb2Se3 admit nonstoichiometric conditions? How modifying the overall Se content affects the structural, optical, and optoelectronic properties of Sb2Se3 thin films, ACS Appl. Mater. Interfaces 14 (2022) 11222–11234, https://doi.org/10.1021/ACSAMI.1C20764.

[32] X. Wen, C. Chen, S. Lu, K. Li, R. Kondrotas, Y. Zhao, W. Chen, L. Gao, C. Wang, J. Zhang, G. Niu, J. Tang, Vapor transport deposition of antimony selenide thin film solar cells with 7.6% efficiency, Nat. Commun. 9 (2018) 1–10, https://doi.org/10.1038/s41467-018-04634-6.

[33] X. Hu, J. Tao, G. Weng, J. Jiang, S. Chen, Z. Zhu, J. Chu, Investigation of electrically-active defects in Sb2Se3 thin-film solar cells with up to 5.91% efficiency via admittance spectroscopy, Sol. Energy Mater. Sol. Cell. 186 (2018) 324–329, https://doi.org/10.1016/j.solmat.2018.07.004.

[34] C. Gao, J. Huang, H. Li, K. Sun, Y. Lai, M. Jia, L. Jiang, F. Liu, Fabrication of Sb2S3 thin films by sputtering and post-annealing for solar cells, Ceram. Int. 45 (2019) 3044–3051, https://doi.org/10.1016/J.CERAMINT.2018.10.155.

[35] M.I. Medina-Montes, Z. Montiel-González, N.R. Mathews, X. Mathew, The influence of film deposition temperature on the subsequent post-annealing and crystallization of sputtered Sb2S3 thin films, J. Phys. Chem. Solid. 111 (2017) 182–189, https://doi.org/10.1016/J.JPCS.2017.07.035.

[36] J. Han, S. Wang, X. Li, H. Tang, Q. Cao, J. Yang, J. Zhu, X. Liu, Z. Li, W. Liu, Alcohol vapor post-annealing for highly efficient Sb2S3 planar heterojunction solar cells, Solar RRL 3 (2019), 1900133, https://doi.org/10.1002/SOLR.201900133.

[37] E. Kask, J. Krustok, S. Giraldo, M. Neuschitzer, S. López-Marino, E. Saucedo, Temperature dependent electrical characterization of thin film Cu$_2$ZnSnSe$_4$ solar cells, J. Phys. D Appl. Phys. 49 (2016), 085101, https://doi.org/10.1088/0022-3727/49/8/085101.

[38] M.E. Uslu, R. Kondrotas, R. Nedzinskas, O. Volobujeva, K. Timmo, M. Kauk-Kuusik, J. Krustok, M. Grossberg, Study of the optical properties of Sb2(Se1-xSx)3 (x = 0–1) solid solutions, Mater. Sci. Semicond. Process. 144 (2022), 106571, https://doi.org/10.1016/J.MSSP.2022.106571.

[39] J.S. Eensalu, A. Katerski, E. Kärber, I.O. Acik, A. Mere, M. Krunks, Jako S. Eensalu, Atanas Katerski, Erki Kärber, Ilona Oja Acik, Arvo Mere, Malle Krunks, Uniform Sb2S3 optical coatings by chemical spray method, Beilstein J. Nanotechnol. 10 (2019) 198–210, https://doi.org/10.3762/bjnano.10.18.

[40] L.Ph Bérubé, G. L'Espérance, A quantitative method of determining the degree of texture of zinc electrodeposits, J. Electrochem. Soc. 136 (1989) 2314–2315, https://doi.org/10.1149/1.2097318.

[41] Z. Li, X. Liang, G. Li, H. Liu, H. Zhang, J. Guo, J. Chen, K. Shen, X. San, W. Yu, R.E. I. Schropp, Y. Mai, 9.2%-efficient core-shell structured antimony selenide nanorod array solar cells, Nat. Commun. 10 (2019) 1–9, https://doi.org/10.1038/s41467-018-07903-6.

[42] Y. Zhou, L. Wang, S. Chen, S. Qin, X. Liu, J. Chen, D.J. Xue, M. Luo, Y. Cao, Y. Cheng, E.H. Sargent, J. Tang, Thin-film Sb2Se3 photovoltaics with oriented one-dimensional ribbons and benign grain boundaries, Nat. Photonics 9 (2015) 409–415, https://doi.org/10.1038/nphoton.2015.78.

[43] N. Spalatu, J. Hiie, R. Kaupmees, O. Volobujeva, J. Krustok, I.O. Acik, M. Krunks, Postdeposition processing of SnS thin films and solar cells: prospective strategy to obtain large, sintered, and doped SnS grains by recrystallization in the presence of a metal halide flux, ACS Appl. Mater. Interfaces 11 (2019) 17539–17554, https://doi.org/10.1021/acsami.9b03213.

[44] C.K. Gan, J.R. Soh, Y. Liu, Large anharmonic effect and thermal expansion anisotropy of metal chalcogenides: the case of antimony sulfide, Phys. Rev. B Condens. Matter 92 (2015), https://doi.org/10.1103/PhysRevB.92.235202.

[45] M.G. Herrmann, R.P. Stoffel, I. Sergueev, H.C. Wille, O. Leupold, M. Ait Haddouch, G. Sala, D.L. Abernathy, J. Voigt, R.P. Hermann, R. Dronskowski, K. Friese, Lattice dynamics of Sb2Se3 from inelastic neutron and X-ray scattering, Phys. Status Solidi 257 (2020), 2000063, https://doi.org/10.1002/PSSB.202000063.

[46] Z.B. Zhao, S.M. Yalisove, Z.U. Rek, J.C. Bilello, Evolution of anisotropic microstructure and residual stress in sputtered Cr films, J. Appl. Phys. 92 (2002) 7183, https://doi.org/10.1063/1.1521791.

[47] S. Mani, T.M. Saif, Mechanism of controlled crack formation in thin-film dielectrics, Appl. Phys. Lett. 86 (2005), 201903, https://doi.org/10.1063/1.1927267.

[48] N. Spalatu, J. Hiie, V. Valdna, M. Caraman, N. Maticiuc, V. Mikli, T. Potlog, M. Krunks, V. Lughi, Properties of the CdCl2 air-annealed CSS CdTe thin films, in: Energy Procedia, Elsevier, 2014, pp. 85–95, https://doi.org/10.1016/j.egypro.2013.12.013.

[49] A. Graf, N. Maticiuc, N. Spalatu, V. Mikli, A. Mere, A. Gavrilov, J. Hiie, Electrical characterization of annealed chemical-bath-deposited CdS films and their application in superstrate configuration CdTe/CdS solar cells, in: Thin Solid Films, Elsevier, 2015, pp. 351–355, https://doi.org/10.1016/j.tsf.2014.11.003.

[50] N. Spalatu, M. Krunks, J. Hiie, Structural and optoelectronic properties of CdCl2 activated CdTe thin films modified by multiple thermal annealing, Thin Solid Films 633 (2017) 106–111, https://doi.org/10.1016/j.tsf.2016.09.042.

[51] R. Scheer, H.-W. Schock, Chalcogenide Photovoltaics, Wiley-VCH Verlag GmbH & Co. KGaA, Weinheim, Germany, 2011, https://doi.org/10.1002/9783527633708.

[52] A. Niemegeers, M. Burgelman, A. de Vos, On the CdS/CuInSe2 conduction band discontinuity, Appl. Phys. Lett. 67 (1998) 843, https://doi.org/10.1063/1.115523.

[53] H. Shiel, O.S. Hutter, L.J. Phillips, J.E.N. Swallow, L.A.H. Jones, T.J. Featherstone, M.J. Smiles, P.K. Thakur, T.L. Lee, V.R. Dhanak, J.D. Major, T.D. Veal, Natural band alignments and band offsets of Sb2Se3Solar cells, ACS Appl. Energy Mater. 3 (2020) 11617–11626, https://doi.org/10.1021/ACSAEM.0C01477/ASSET/IMAGES/LARGE/AE0C01477_0010 (JPEG).

[54] T. Walter, R. Herberholz, C. Müller, H.W. Schock, Determination of defect distributions from admittance measurements and application to Cu(In,Ga)Se2 based heterojunctions 80 (1996) 4411–4420, https://doi.org/10.1063/1.363401.

[55] L. Zhang, W. Lian, X. Zhao, Y. Yin, T. Chen, C. Zhu, Sb2S3Seed-Mediated growth of low-defect Sb2S3on a TiO2Substrate for efficient solar cells, ACS Appl. Energy Mater. 3 (2020) 12417–12422, https://doi.org/10.1021/ACSAEM.0C02400/ASSET/IMAGES/LARGE/AE0C02400_0006 (JPEG).

[56] Z. Cai, C.M. Dai, S. Chen, Intrinsic defect limit to the electrical conductivity and a two-step p-type doping strategy for overcoming the efficiency bottleneck of Sb2S3-based solar cells, Solar RRL 4 (2020), 1900503, https://doi.org/10.1002/SOLR.201900503.

[57] M. Grossberg, O. Volobujeva, A. Penežko, R. Kaupmees, T. Raadik, J. Krustok, Origin of photoluminescence from antimony selenide, J. Alloys Compd. 817 (2020), 152716, https://doi.org/10.1016/j.jallcom.2019.152716.